

Structural Information from Ion Mobility Measurements: Effects of the Long-Range Potential

M. F. Mesleh, J. M. Hunter,[†] A. A. Shvartsburg, G. C. Schatz,* and M. F. Jarrold*

Department of Chemistry, Northwestern University, 2145 Sheridan Road, Evanston, Illinois 60208

Received: June 4, 1996; In Final Form: August 6, 1996[⊗]

In a number of recent studies, information about the structure of large polyatomic ions has been deduced from gas phase ion mobility measurements by comparing mobilities measured in helium to those estimated for assumed geometries using a hard sphere projection approximation. To examine the validity of this approach, we have compared mobilities calculated using the hard sphere projection approximation for a range of fullerenes (C₂₀–C₂₄₀) to those determined from trajectory calculations with a more realistic He–fullerene potential. The He–fullerene potential we have employed, a sum of two-body 6-12 interactions plus a sum of ion-induced dipole interactions, was calibrated using the measured mobility of C₆₀⁺ in helium over an 80–380 K temperature range. For the systems studied, the long-range interactions between the ion and buffer gas have a small, less than 10%, effect on the calculated mobility at room temperature. However, the effects are not insignificant, and in many cases it will be necessary to consider the long-range interactions if the correct structural assignments are to be made from measured ion mobilities.

Introduction

The mobility of a gas phase ion is a measure of how rapidly it moves through a buffer gas under the influence of an electric field. The mobility depends on the average collision cross section, which in turn depends on the geometry.¹ Recently, ion mobility measurements have been used to deduce structural information about large polyatomic ions.² In these studies the measured mobility is compared to mobilities estimated for assumed geometries using a hard sphere projection approximation.³ In this paper we describe studies designed to examine the validity of this approach. Specifically, we examine how the long-range potential between the polyatomic ion and buffer gas affects the room temperature mobility. To accomplish this, we have compared mobilities determined from trajectory calculations with a realistic potential to mobilities estimated using the hard sphere projection approximation. We also consider the influence of ion structure, in particular atomic-level surface roughness, on the mobilities. Fullerenes were employed as models to examine these issues because geometries are available from theory for a wide range of shapes and sizes and because we could calibrate the potential using the experimentally known structure for C₆₀. Book et al.⁴ have previously reported a study of the effects of vibrational motion on mobilities calculated using the hard sphere projection approximation. They found vibrational effects to be negligible at room temperature for rigid geometries such as fullerenes.

Mobility Calculations

The mobility, K , of a gas phase ion is defined by $K = v_D/E$ where v_D is the drift velocity and E is the electric field. The zero-field mobility can be calculated from^{5,6}

$$K = \frac{(18\pi)^{1/2}}{16} \left[\frac{1}{m} + \frac{1}{m_B} \right]^{1/2} \frac{ze}{(k_B T)^{1/2} \Omega_{\text{avg}}^{(1,1)}} \frac{1}{N} \quad (1)$$

In this expression, m is the mass of the ion, m_B is the mass of

a buffer gas atom, N is the buffer gas number density, ze is the ion's charge, and $\Omega_{\text{avg}}^{(1,1)}$ is the orientationally averaged collision integral. T is the effective temperature given by $T_{\text{BG}} + m_B v_D^2 / 3k_B$,⁷ where v_D is the drift velocity, T_{BG} is the buffer gas temperature, and the second term accounts for the small perturbation (typically less than 1 K) caused by the presence of the drift field. The collision integral^{6,8} is related to the scattering angle, the angle between the trajectory before and after a collision between the ion and a buffer gas atom. The collision integral is calculated by averaging over the impact parameter and relative velocity, and the average collision integral, $\Omega_{\text{avg}}^{(1,1)}$, is obtained by averaging the collision integral over all possible collision geometries:

$$\Omega_{\text{avg}}^{(1,1)} = \frac{1}{8\pi^2} \int_0^{2\pi} d\theta \int_0^\pi d\phi \sin \phi \int_0^{2\pi} d\gamma \frac{\pi \left(\frac{\mu}{k_B T} \right)^3 \int_0^\infty dg e^{-\mu g^2 / (2k_B T)} g^5 \int_0^\infty db 2b(1 - \cos \chi(\theta, \phi, \gamma, g, b)) \quad (2)$$

In this expression θ , ϕ , and γ are three angles that define the collision geometry between the polyatomic ion and the buffer gas atom, $\chi(\theta, \phi, \gamma, g, b)$ is the scattering angle, g is the relative velocity, and b is the impact parameter. Except for simple, spherically symmetric potentials, the scattering angle must be calculated by numerical integration of the equations of motion. The potential employed in the work described here is

$$\Phi(\theta, \phi, \gamma, b, r) = 4\epsilon \sum_i^n \left[\left(\frac{\sigma}{r_i} \right)^{12} - \left(\frac{\sigma}{r_i} \right)^6 \right] - \frac{\alpha \left(\frac{ze}{n} \right)^2 \left[\left(\sum_i^n \frac{x_i}{r_i^3} \right)^2 + \left(\sum_i^n \frac{y_i}{r_i^3} \right)^2 + \left(\sum_i^n \frac{z_i}{r_i^3} \right)^2 \right] \quad (3)$$

The first term in this expression is a sum of two-body 6-12 interactions, and the second term is the ion-induced dipole interaction. We have assumed that the charge is distributed equally over the ion, which seems appropriate for the fullerenes considered here. In eq 3, ϵ and σ are the Lennard-Jones parameters (ϵ is the well depth and σ is the distance where the potential becomes positive), α is the polarizability of the buffer

[†] Present address: SRI International, Menlo Park, CA 94025.

[⊗] Abstract published in *Advance ACS Abstracts*, September 15, 1996.

gas atom (helium), n is the number of atoms in the ion, and r_i , x_i , y_i , and z_i are coordinates that define the relative positions of the atoms with respect to the buffer gas atom. Trajectories were calculated using a Runge–Kutta–Gill initiator and an Adams–Moulton predictor–corrector propagator. Energy conservation for all trajectories was better than 0.5%.

Accurate evaluation of the average collision integral in the way described above is a long and computationally expensive process, and it has not been performed in this way for polyatomic ions prior to the work reported here. In recent work the collision integral has been approximated by

$$\Omega_{\text{avg}}^{(1,1)} \approx \frac{1}{8\pi^2} \int_0^{2\pi} d\theta \int_0^\pi d\phi \sin\phi \int_0^{2\pi} d\gamma \pi b_{\text{min}}^2 \quad (4)$$

where b_{min} is the minimum impact parameter for a collision geometry defined by θ , ϕ , and γ that avoids a hard sphere contact with any atom in the cluster. We will refer to this as the hard sphere projection approximation. Although it is clear that eq 4 ignores the long-range interactions between the ion and the buffer gas atom, it is less obvious that this approach also ignores all the details of the scattering process and effectively replaces the collision integral with the collision integral of a sphere of the same average projection as that of the polyatomic ion. Even with the hard sphere potential for intermolecular interactions, a polyatomic ion should be treated as a collection of spheres. We have constructed a rigorous hard sphere scattering model that accurately accounts for the details of the scattering process. The results of its application to clusters of different shapes are reported elsewhere.⁹ For the purposes of the present discussion it is sufficient to state that, for any finite, locally convex surface, the exact orientationally averaged hard sphere collision integral is equal to the orientationally averaged projection, and therefore, the hard sphere projection approximation is exact. However, this does not hold for bodies with partially concave surfaces, where multiple scattering and shadowing can occur. Since closed cage fullerenes are close to ideal convex bodies, the collision integrals calculated using the hard sphere projection approximation deviate only slightly from those calculated using the rigorous hard sphere scattering model. For example, the deviations are -1.1% for C_{20} and $+1.4\%$ for C_{240} (*S*). However, much larger deviations, more than 10%, can occur for geometries with grossly concave surfaces, such as cups.⁹

To perform calculations of the mobilities along the lines described above, it is necessary to define values for the Lennard–Jones parameters, ϵ and σ , for the more realistic potential and a value for the contact distance for the hard sphere projection approximation. Since these quantities are not well-defined, we have employed the measured mobility of C_{60}^+ , which has a well-known geometry,¹⁰ to define these parameters. In the case of the realistic potential it is necessary to compare with mobilities measured as a function of temperature in order to unambiguously define ϵ and σ .

Experimental Measurements

The injected ion drift tube apparatus used in these studies has been described in detail previously.¹¹ The carbon clusters were generated by pulsed laser vaporization of a carbon rod in a continuous flow of helium buffer gas. Ions that exit the source were focused into a quadrupole mass spectrometer, which is used to select a specific cluster ion. The mass-selected cluster ions were then focused into a low-energy ion beam and injected into the drift tube. The drift tube is 7.6 cm long. It can be cooled with liquid nitrogen or heated with electrical heaters.

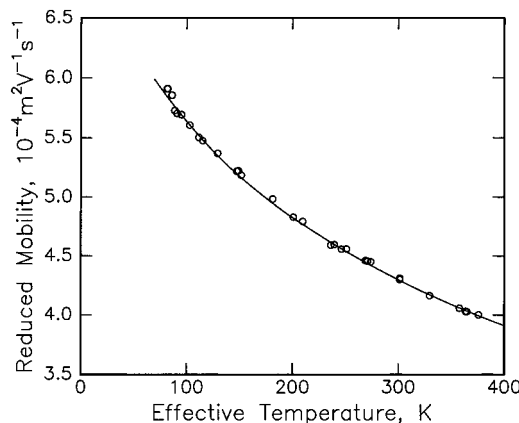


Figure 1. Plot of mobilities measured for C_{60}^+ over an 80–380 K temperature range. The points are the experimental data, and the line is a spline fit to mobilities calculated with the He– C_{60}^+ Lennard–Jones plus ion-induced dipole potential described in the text. The solid line is the optimized fit with $\sigma = 3.068 \text{ \AA}$ and $\epsilon = 1.34 \text{ meV}$.

The temperature was monitored by two thermocouples. The maximum temperature gradient across the drift tube was 3 K. The helium buffer gas pressure was measured by a capacitance manometer. Tests performed at low temperature indicate that thermal transpiration introduces less than 1% error into the pressure measurements. After traveling across the drift tube, some of the ions exit through a small aperture and are focused into a second quadrupole mass spectrometer. At the end of this quadrupole, the ions are detected by an off-axis collision dynode and dual microchannel plates. To measure mobilities, 50 μs pulses of size-selected clusters are injected into the drift tube and their arrival time distribution is recorded at the detector using a multichannel analyzer. The drift time distribution is then determined by subtracting, from the time scale, the time it takes for the ion to travel from the exit of the drift tube to the detector. Mobilities were determined from the drift time distributions by fitting the measured distributions with those calculated from solution of the transport equation for ions in the drift tube:⁵

$$F(t) = \int dt_p P(t_p) \frac{C(v_D + L/(t - t_p))}{(DT)^{1/2}} \times \left[1 - \exp\left(\frac{-r_0^2}{4D(t - t_p)}\right) \right] \exp\left(\frac{-(L - v_D(t - t_p))^2}{4D(t - t_p)}\right) \quad (5)$$

treating the drift velocity, v_D , as an adjustable parameter. In eq 5, r_0 is the radius of the entrance aperture, L is the length of the drift tube, $P(t_p) dt_p$ is the distribution function of the pulse of ions entering the drift tube, C is a constant, and D is the diffusion constant, which under the low field conditions employed here is given by $Kk_B T/ze$. The reduced mobility is then determined from

$$K_0 = \frac{v_D}{E} \frac{P}{760} \frac{273.2}{T_{\text{BG}}} \quad (6)$$

where P is the buffer gas pressure.

Results

The mobilities measured for C_{60}^+ over an 80–380 K temperature range are plotted in Figure 1. The results shown in the figure were recorded in two time intervals separated by six months. Von Helden et al. have also performed measurements of the mobilities of C_{60}^+ as a function of temperature.¹²

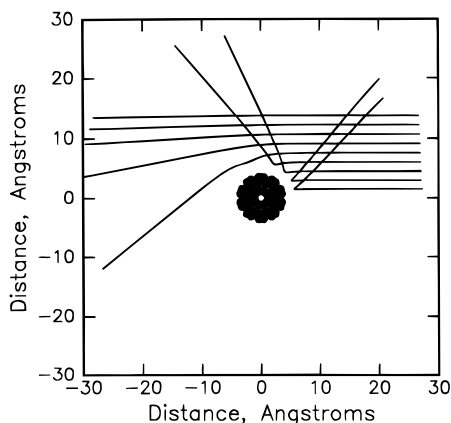


Figure 2. Plot of some He- C_{60}^+ trajectories calculated using the optimized He- C_{60}^+ Lennard-Jones plus ion-induced dipole potential (see text). The trajectories were run with a collision energy of $k_B T$ with $T = 298$ K.

Their results are in reasonable agreement with those shown in Figure 1. As a test of the accuracy of our mobility measurements, mobilities were measured for C_{60}^+ generated from laser-desorbed fullerene films using a new high-resolution ion mobility apparatus that we have recently constructed.¹³ The room temperature, 298 K, mobility for C_{60}^+ measured using this new apparatus agreed with that measured with the injected ion drift tube apparatus to within 1%.

The solid line through the experimental results in Figure 1 was obtained by fitting the measured mobilities with the trajectory simulations, treating the Lennard-Jones parameters σ and ϵ as adjustable. The fit to the experimental data is clearly very good and is much better than the corresponding hard sphere result.¹² The optimum values determined from the fit were $\sigma = 3.068$ Å and $\epsilon = 1.34$ meV. The values for σ and ϵ deduced above can be compared with values obtained from the Lennard-Jones parameters for carbon and helium using⁶ $\sigma_{\text{He-C}} = \sigma_{\text{He-He}} + \sigma_{\text{C-C}}$ and $\epsilon_{\text{He-C}} = (\epsilon_{\text{He-He}}\epsilon_{\text{C-C}})^{1/2}$. With the Lennard-Jones parameters for helium⁶ and Lennard-Jones parameters deduced for carbon from the interlayer interactions in graphite,¹⁴ the values obtained were $\sigma_{\text{He-C}} = 2.98$ Å and $\epsilon_{\text{He-C}} = 1.46$ meV. These values are in good agreement with those obtained by fitting the mobility data for C_{60}^+ . A value for the contact distance for the hard sphere projection approximation was deduced by fitting the room temperature, 298 K, mobility of C_{60}^+ . The value obtained was 2.86 Å. This value is slightly larger than employed previously because the MNDO coordinates¹⁵ used have been scaled by 0.9884 to match the diameter of C_{60} deduced from X-ray and electron diffraction studies.¹⁰

Figure 2 shows examples of trajectories calculated for He- C_{60}^+ scattering. Trajectories are shown for a range of impact parameters for a collision energy given by $k_B T$ with $T = 298$ K. The effect of the long-range interactions between C_{60}^+ and He, a significant deflection of the trajectories, is apparent at large impact parameters even at room temperature. At lower temperatures, where the attractive interactions become more important, orbiting collisions with multiple impacts occur. Figure 3 shows a plot of the orientationally averaged effective potential for He- C_{60}^+ obtained using eq 3 with $\sigma = 3.068$ Å and $\epsilon = 1.34$ meV. The average He- C_{60}^+ potential has a minimum of 10.3 meV at 3.03 Å from the surface of the fullerene. Thus, the average He- C_{60}^+ potential is around 8 times deeper than that for a single He-C two-body interaction. Comparison to the average potential determined without the ion-induced dipole contribution shows that the ion-induced dipole interaction is responsible for only around 10% of the He- C_{60}^+ potential at the minimum. The He- C_{60}^+ potential is around 8

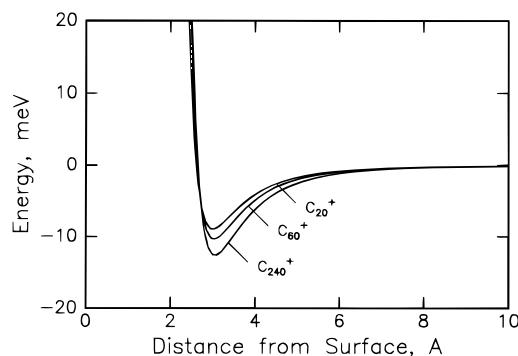


Figure 3. Plot of the optimized orientationally averaged He- C_{60}^+ Lennard-Jones plus ion-induced dipole potential described in the text. Orientationally averaged potentials are also shown for He- C_{20}^+ and He- C_{240}^+ (S).

times deeper than a single He-C two-body interaction because the helium interacts, to some extent, with all the carbon atoms in C_{60}^+ . Orientationally averaged effective potentials are also shown in Figure 3 for C_{20}^+ (calculated using C_{20} MNDO coordinates¹⁶) and C_{240}^+ (calculated using coordinates for the S isomer of York et al.¹⁷). We selected these fullerenes because they are nearly spherical, and so it is easy to calculate an orientationally averaged effective potential as a function of the distance from the fullerene surface. As can be seen from the figure, the potential minimum becomes deeper with increasing fullerene size. The contribution of the ion-induced dipole interaction to the effective potential decreases with increasing cluster size. Thus, the ion-induced dipole interactions minimize the variations in the effective potentials with fullerene size.

Von Helden et al. have recently reported simulations of the temperature dependence of the mobility of C_{60}^+ in He.¹² The approach they employ is quite different from that adopted here, where we sum the He-C interactions to obtain an effective He-fullerene potential and then run trajectories using this potential. Instead, von Helden et al. assume that the He interacts with only a single carbon atom in the cluster and use collision integrals tabulated as a function of temperature for atom-atom collisions with a 12-6-4 potential to define a contact distance as a function of temperature. This approach ignores the fact that the effective potential receives contributions from many C-He interactions and that the helium, particularly at low temperatures, interacts with many carbon atoms during a collision.

As a further check of the reliability of the potential deduced here, we have compared it with several He-graphite potentials. Although the chemical bonding in fullerenes and graphite is not identical, He-graphite seems to be the best available system for comparison. Figure 4 shows the orientationally averaged effective He- C_{60} potential (determined using eq 3 with $\sigma = 3.068$ Å and $\epsilon = 1.34$ meV but without the ion-dipole interaction) and several different laterally averaged He-graphite potentials obtained from fitting experimental data. The He- C_{60} potential is shallower than the graphite-helium potentials because the surface of the fullerene is curved and because with graphite the helium can interact with more carbon atoms. To facilitate comparison with the He-graphite potentials, we have calculated a laterally averaged effective He-graphite potential using the Lennard-Jones parameters deduced from the mobility measurements. The result is shown as the solid line labeled *LJ graphite slab* in Figure 4. This potential can be compared with He-graphite potentials deduced from helium-scattering experiments, which are shown as the dashed lines. The dashed line labeled *JLB* is the He-graphite potential of Joly, Lhuillier, and Brami¹⁸ and that labeled *RSJ* is due to Ruiz, Scoles, and

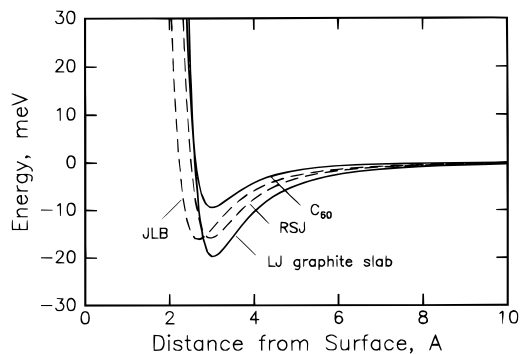


Figure 4. Comparison of the orientationally averaged He–C₆₀ potential with laterally averaged He–graphite potentials. The solid line labeled *LJ graphite slab* was obtained using the Lennard-Jones parameters deduced from the mobility measurements. The dashed lines show the He–graphite potentials of Joly, Lhuillier, and Brami (*JLB*) and Ruiz, Scoles, and Jonsson (*RSJ*) obtained from He–graphite scattering experiments.

Jonsson.¹⁹ The helium-scattering experiments provide the He–graphite bound state energies, which give a good measure of the shape and depth of the potential but are insensitive to the He–graphite distance at the potential minimum. The *JLB* potential is a fairly simple empirical potential that fixes the average He–graphite distance in the ground state at 2.85 Å, the value determined from neutron-scattering studies of helium adsorbed on graphite.²⁰ The *RSJ* potential is a more sophisticated potential incorporating damping functions.²¹ The mobility studies reported here are more sensitive to the location of the repulsive part of the He–C potential. The potential deduced from the mobility studies is clearly in better agreement with the *RSJ* potential. The minimum in the *JLB* potential occurs at a distance shorter than those of the other potentials. One reason for this discrepancy is that the He–graphite distance in the *JLB* potential is fixed at the distance determined for helium adsorbed on graphite. He adsorbs on graphite over hexagonal sites where the helium is closer to the surface than the laterally averaged He–graphite distance. However, the He–graphite potential is only weakly corrugated, and according to our estimates, this accounts for less than a third of the discrepancy. So it may be desirable to re-evaluate the He–graphite distance deduced from the neutron-scattering data, particularly since the simulations of the neutron-scattering data used to extract the He–graphite distance were not in good agreement with the measured data.²⁰ Finally, the *LJ graphite slab* potential is slightly deeper than the potentials deduced from the He–graphite scattering experiments. This is probably a reflection of the crudeness of the relatively simple two-body potential employed in this work. We are currently evaluating more sophisticated He–C potentials with the goal of simultaneously fitting the mobility data and the He–graphite scattering results.

Information about the interaction between noble gas atoms and fullerenes is important in studies of endohedral complexes of these atoms.²² The potentials used by researchers in this area are constructed from sums of pairwise Lennard-Jones interactions, similar to the potentials employed here. However, the parameters for the Lennard-Jones interactions were assumed to be the same as those calculated for noble gas atoms interacting with carbon atoms in aromatic rings;²³ for helium $\sigma = 3.33$ Å and $\epsilon = 1.61$ meV or 1.63 meV. These values lead to a He–fullerene potential that is deeper and extends further than the one derived here. Mobilities calculated with this potential deviate from the measured mobilities by 15–20%.

Table 1 shows inverse mobilities calculated from the trajectory calculations and estimated using the hard sphere projection

TABLE 1: Comparison of the Inverse Mobilities Calculated for Near-Spherical Fullerenes C₂₀⁺, C₆₀⁺, and C₂₄₀⁺ (*S*) Using the Realistic Fullerene–He Potential and the Hard Sphere Projection Approximation^a

fullerene	(mobility) ⁻¹ hard sphere m ⁻² V s	(mobility) ⁻¹ Lennard-Jones m ⁻² V s	HSA/LJ
C ₂₀ ⁺	1324	1260	1.051
C ₆₀ ⁺	2321	2321	1.000
C ₂₄₀ ⁺ (<i>S</i>) ^b	5749	6013	0.956

^a Calculations were performed with a temperature of 298 K. ^b *S* isomer of C₂₄₀ from ref 17.

approximation for C₂₀⁺, C₆₀⁺, and C₂₄₀⁺. It is convenient to consider the inverse mobilities here because the inverse mobility is proportional to the collision integral. The expression for the mobility, eq 1, is derived from the first term in the Sonine expansion of the Boltzmann transport equation⁶ using the Nernst–Townsend relationship.⁵ We have evaluated second-order corrections for mobilities calculated with the realistic potential. This involves calculating further collision integrals, $\Omega^{(1,2)}$, $\Omega^{(1,3)}$, and $\Omega^{(2,2)}$ as outlined in Hirschfelder, Curtiss, and Bird.⁶ For the systems studied here, the second-order corrections were negligible. We have employed two different schemes to evaluate the integrals over orientation, velocity, and impact parameter in eq 2. Both schemes yield similar results. The results presented in the tables were evaluated by Monte Carlo integration over orientation and impact parameter and by a numerical integration over velocity. The values shown in Table 1 are the average of four determinations, and the standard error of the mean was less than 0.3% in all cases.

In Table 1, inverse mobilities calculated for C₆₀⁺ using the realistic potential and the hard sphere projection approximation agree because both methods were calibrated for C₆₀⁺. However, for C₂₀⁺ and C₂₄₀⁺ there are differences of around 5% between the inverse mobilities calculated using the different methods. For C₂₀⁺ the hard sphere projection approximation overestimates the inverse mobility by 5%, and for C₂₄₀⁺ the inverse mobility is underestimated. Calculations performed for other fullerenes with 20–240 atoms show that the deviations are systematic. This systematic deviation is due primarily to two related factors, both of which lead to larger scattering angles and larger inverse mobilities with increasing size. First, as is clear from the potentials shown in Figure 3, as the fullerene becomes larger, the effective potential experienced by the helium becomes more strongly attractive. And second, the helium interacts with the larger fullerenes over a longer distance. Consider a grazing collision with an impact parameter set at some distance from the fullerene surface. As the fullerene increases in size, the helium interacts with it for a longer portion of the trajectory, so the scattering angle increases, leading to a larger inverse mobility.

Comparison of the calculated mobilities with mobilities measured for fullerenes other than C₆₀ and C₇₀ is potentially misleading because the geometries are not known with certainty. In Table 2 we compare calculated mobilities for C₃₄⁺, C₆₀⁺, and C₂₄₀⁺ with measured mobilities. For C₂₀⁺ the fullerene isomer has not been observed, and so a comparison is not possible. For C₃₄⁺ we have used scaled²⁴ MNDO coordinates,¹⁶ and for C₂₄₀⁺ calculated inverse mobilities are shown for two different geometries: a HF polyhedrally faceted geometry from Scuseria²⁵ and the scaled MNDO coordinates for an icosahedral geometry from Bakowies and Thiel.²⁶ The nearly spherical C₂₄₀ *S* isomer of York et al.¹⁷ employed above resulted from calculations performed using the local density approximation and the divide and conquer technique.²⁷ Several more recent

TABLE 2: Comparison of the Inverse Mobilities Calculated for C₃₄⁺, C₆₀⁺, and C₂₄₀⁺ (PF) Fullerenes Using the Realistic Fullerene–He Potential and the Hard Sphere Projection Approximation with the Measured Inverse Mobilities^a

fullerene	(mobility) ⁻¹ hard sphere m ⁻² V s	(mobility) ⁻¹ Lennard-Jones m ⁻² V s	(mobility) ⁻¹ measured m ⁻² V s
C ₃₄ ⁺	1709	1664	1664
C ₆₀ ⁺	2321	2321	2321
C ₂₄₀ ⁺ (PF) ^b	5741	6014	5900
C ₂₄₀ ⁺ (I _h) ^c	5731	6003	5900

^a The calculations were performed with a temperature of 298 K. ^b Polyhedrally faceted geometry for C₂₄₀ from ref 25. ^c I_h geometry for C₂₄₀ from ref 26.

calculations find the spherical isomer is not a local minimum and suggest that a polyhedrally faceted geometry is the ground state.^{25,28} Inverse mobilities calculated using the realistic potential for C₃₄⁺ are in exact agreement with the measured mobility. This precise agreement is probably fortuitous because the standard error of the mean of the calculated mobilities is 0.2–0.3%, and the uncertainty in the measured mobilities is ±0.5%. The inverse mobility estimated for C₃₄⁺ using the hard sphere projection approximation deviates from the experimental value by +3.8%. This deviation results from the effects of the long-range potential. The two C₂₄₀ isomers shown in Table 2 have calculated inverse mobilities that deviate from the measured mobility by +1.9% and +1.7%. Mobilities calculated with the hard sphere approximation deviate from the measured mobility by –2.7% and –2.9%. It is not clear why the inverse mobilities calculated for the C₂₄₀ isomers with the realistic potential are not in better agreement with the experimental value. It is possible that the theoretical studies have not yet identified the lowest energy geometry, that the lowest energy geometry is not present in the experiments, or that the deviation is due to the crudeness of the potential we have employed in this work. The spherical *S* isomer of York et al.¹⁷ has a calculated inverse mobility (see Table 1) that is almost identical with the other two isomers in Table 2. However, a polyhedrally faceted isomer of York et al.,¹⁷ their *P* isomer, has a calculated inverse mobility of 6231 m⁻² V s, which is substantially different from the polyhedrally faceted geometries shown in Table 2.

Conclusions

The results presented here show that there are small systematic variations between the mobilities calculated with a realistic intermolecular potential and those estimated from the widely used hard sphere projection approximation. The deviations result from the long-range potential between the ion and buffer gas atom. Although the deviations are not large, they are large enough that incorrect assignments of the geometries could be made, particularly for clusters of heavier, more polarizable atoms where the long-range interactions are expected to be stronger. Furthermore, larger deviations may result for nonspherical geometries where the hard sphere approximation fails to account for the details of the scattering process.

Acknowledgment. We gratefully acknowledge the support of this work by the National Science Foundation (Grant

Numbers CHE-9306900 and CHE-9527677) and the Petroleum Research Fund administered by the American Chemical Society. We are also grateful to Professor W. Yang and his collaborators for providing coordinates for the *S* and *P* isomers of C₂₄₀, to Professor G. Scuseria for providing coordinates for his polyhedrally faceted C₂₄₀ geometry, and to Professor W. Thiel for providing coordinates for his icosahedral C₂₄₀ geometry.

References and Notes

- (1) Hagen, D. F. *Anal. Chem.* **1979**, *51*, 870. Karpas, Z.; Cohen, M. J.; Stimac, R. M.; Wernlund, R. F. *Int. J. Mass Spectrom. Ion Processes* **1986**, *83*, 163.
- (2) von Helden, G.; Hsu, M. T.; Kemper, P. R.; Bowers, M. T. *J. Chem. Phys.* **1991**, *95*, 3835. von Helden, G.; Hsu, M.-T.; Gotts, N.; Bowers, M. T. *J. Phys. Chem.* **1993**, *97*, 8192. Jarrold, M. F. *J. Phys. Chem.* **1995**, *99*, 11.
- (3) Jarrold, M. F.; Constant, V. A. *Phys. Rev. Lett.* **1992**, *67*, 2994.
- (4) Book, L. D.; Xu, C.; Scuseria, G. E. *Chem. Phys. Lett.* **1994**, *222*, 281.
- (5) Mason, E. A.; McDaniel, E. W. *Transport Properties of Ions in Gases*; Wiley: New York, 1988.
- (6) Hirschfelder, J. O.; Curtiss, C. F.; Bird, R. B. *Molecular Theory of Gases and Liquids*; Wiley, New York, 1954.
- (7) See ref 5, p 148.
- (8) Note that the definition of the collision integral employed here differs from that given by Hirschfelder, Curtiss, and Bird.⁶ Following Mason and McDaniel,⁵ a factor of $(k_B T / 2\pi\mu)^{1/2}$ present in the definition of Hirschfelder, Curtiss, and Bird is incorporated into eq 1 rather than in the equation for the collision integral. With this formalism the collision integral for a hard sphere is equivalent to the hard sphere collision cross section, πb^2 .
- (9) Shvartsburg, A. A.; Jarrold, M. F. *Chem. Phys. Lett.*, in press.
- (10) Liu, S.; Lu, Y.-J.; Kappes, M. M.; Ibers, J. A. *Science* **1991**, *254*, 408. Hedburg, K.; Hedburg, L.; Bethune, D. S.; Brown, C. A.; Dorn, H. C.; Johnson, R. D.; de Vries, M. *Science* **1991**, *254*, 410.
- (11) Jarrold, M. F.; Bower, J. E.; Creegan, K. M. *J. Chem. Phys.* **1989**, *90*, 3615.
- (12) von Helden, G.; Wyttenbach, T.; Bowers, M. T. *Int. J. Mass Spectrom. Ion Processes* **1995**, *146/147*, 349.
- (13) Dugourd, P.; Hudgins, R. R.; Clemmer, D. E.; Jarrold, M. F. *Rev. Sci. Instrum.*, submitted.
- (14) Crowell, A. D. *J. Chem. Phys.* **1958**, *29*, 446. Crowell, A. D.; Steele, R. B. *J. Chem. Phys.* **1961**, *34*, 1347. Steele, W. A. *Surf. Sci.* **1973**, *36*, 317.
- (15) Raghavachari, K. Private communication.
- (16) Shelimov, K. B. Private communication.
- (17) York, D.; Lu, J. P.; Yang, W. *Phys. Rev. B* **1994**, *49*, 8526.
- (18) Joley, F.; Lhuillier, C.; Brami, B. *Surf. Sci.* **1992**, *264*, 419.
- (19) Ruiz, J. C.; Scoles, G.; Jonsson, H. *Chem. Phys. Lett.* **1986**, *129*, 139.
- (20) Caneiro, K.; Passell, L.; Thomlinson, W.; Taub, H. *Phys. Rev. B* **1981**, *24*, 1170.
- (21) Tang, K. T.; Toennies, J. P. *J. Chem. Phys.* **1984**, *80*, 3726.
- (22) DiCamillo, B. A.; Hettich, R. L.; Guiochon, G.; Compton, R. N.; Saunders, M.; Jimenez-Vazquez, H. A.; Khong, A.; Cross, R. J. *J. Phys. Chem.* **1996**, *100*, 9197. Pang, L.; Brisse, F. J. *J. Phys. Chem.* **1993**, *97*, 8562. Son, M. S.; Sung, Y. K. *Chem. Phys. Lett.* **1995**, *245*, 113.
- (23) Amos, A.; Palmer, T. F.; Walters, A.; Burrows, B. L. *Chem. Phys. Lett.* **1990**, *172*, 503.
- (24) The coordinates obtained from MNDO calculations were scaled by 0.9884. Scaling the MNDO C₆₀ coordinates by this amount brings the average distance from the center into agreement with that determined from X-ray and electron diffraction studies.¹⁰
- (25) Scuseria, G. E. *Chem. Phys. Lett.* **1995**, *243*, 193.
- (26) Bakowies, D.; Thiel, W. *J. Am. Chem. Soc.* **1991**, *113*, 3704.
- (27) Wang, W. *Phys. Rev. Lett.* **1991**, *66*, 1438.
- (28) Bakowies, D.; Buhl, M.; Thiel, W. *J. Am. Chem. Soc.* **1995**, *117*, 10113. Bakowies, D.; Buhl, M.; Thiel, W. *Chem. Phys. Lett.* **1995**, *247*, 491.

JP961623V